Research Article
Vol. 60, No. 5 / 10 February 2021 / Applied Optics 1283

applied optics

Impact of microvibration on the optical performance of an airborne camera

Jieqiong Lin,[1] Yan Zhou,[1] Haitao Wang,[1] Yan Gu,[1,*] Minghui Gao,[2] Xin Guo,[1] and Haibo Xu[1]

[1]Key Laboratory of Micro/Nano and Ultra-Precision Manufacturing of Jilin Province, School of Mechatronic Engineering, Changchun University of Technology, Changchun, 130012, China
[2]China Changchun Institute of Optics, Fine Mechanics and Physics, Chinese Academy of Sciences, Changchun, 130033, China
*Corresponding author: guyan@ccut.edu.cn

Received 29 September 2020; revised 11 January 2021; accepted 11 January 2021; posted 12 January 2021 (Doc. ID 411299); published 5 February 2021

Aiming to investigate the connection between camera structure and optical systems, a comprehensive analysis needs to be performed for the airborne camera. An integrated analysis method was proposed to design and analyze optical and mechanical structures. Based on the designed small airborne camera, the impact of microvibration on the optical performance of the airborne camera was studied by integrated optomechanical analysis. In addition, the change of optical surface accuracy was analyzed. First, static and dynamic analysis of the designed airborne camera was performed to verify the stability of the camera structure and obtain the data for integrated optomechanical analysis. Then, a calculation method for rigid body displacement was proposed, and the impact of rigid body displacements on the optical system was analyzed. To evaluate the change of surface accuracy, the parameters root mean square (RMS) and peak to valley (PV) were calculated by fitting the surface distortion data. Based on the Zernike polynomial coefficients, the response of the optical system was calculated and analyzed utilizing ZEMAX to analyze the impact of microvibration on the optical performance of the airborne camera. The analysis results show that microvibration has no significant impact on optical performance of the designed small airborne camera. Finally, the analysis results were verified through experiments.

https://doi.org/10.1364/AO.411299

1. INTRODUCTION

Airborne cameras with high resolution are susceptible to deformations caused by complex condition loads (e.g., temperature fluctuations, vibration, gravity). It is indispensable to analyze their dynamic response and reliability. In the traditional structural analysis of the airborne camera, the analysis is usually made to verify whether the deformation of the optical element meets the tolerances given in the optical design [1,2]. However, this method cannot analyze the effect of deformation of the optical element on optical performance. Therefore, a comprehensive analysis method needs to analyze the impact of deformation of the optical element on optical performance [3,4]. Compared with traditional structural analysis, integrated optomechanical analysis can analyze the influence of external disturbances on the optical system, which can be used to optimize the optomechanical structure. Recently, more and more attention has been focused on the integrated optomechanical analysis of high-resolution optical systems [5]. Integrated optomechanical analysis has been widely used in the optimization of space mirror structure, thermal analysis of cameras, and adaptive optical systems. For example, Liu *et al.* modified the thermal control system, which can improve the thermal control performance of the system [1]. This method builds a relationship between the thermal control system and optical performance by integrated optomechanical analysis. The advantage of integrated optomechanical analysis is that it can gain insight into the interdisciplinary design relationship between optical component deformation and optical performance. Rausch *et al.* investigated the aberrations caused by thermal deformations, gravitational release, and alignment errors that occur during the deployment procedure of large space telescopes by using the integrated optomechanical analysis method. Then, they developed an active optics system to decrease the requirements for stability of the thermal and mechanical properties of the optical system [6]. This approach provides rational support for structure reliability optimization design of a large space mirror. With the increasing demand for high-resolution airborne cameras, much work has been carried out on integrated optomechanical analysis. For example, Camilo *et al.*, taking advantage of optical material properties, presented a technique to determine wavefront error and polarization changes [7]. Xue *et al.*, utilizing integrated optomechanical analysis, proposed an analysis and experimental method for thermal control system of an aerial camera, which can be used to analyze the impact of internal thermal environment on the performance of an optical system [8]. Doyle discussed how to optimize an optomechanical structure subjected to vibrational loading by utilizing mechanical and optical analysis software [9]. He pointed out that analyzing the impact of vibration on optical performance was an important step in camera optimization. Just like temperature, microvibration is unavoidable in the working environment; therefore, it is necessary to investigate the impact of microvibration on the optical performance of the airborne camera.

Microvibration will cause surface distortion and rigid body displacement of optical elements. As important parameters, surface distortion and rigid body displacement reflect the change of surface characteristics caused by microvibration. Based on the data of finite element analysis (FEA), the surface distortion and rigid body displacements of the optical elements can be calculated to analyze the changes in the surface characteristics. Furthermore, establishing an integrated optomechanical analysis interface is an important part of analyzing the impact of microvibration on the imaging quality of airborne cameras. Zernike polynomials can be used to transform deformed surface nodal data into an optics format. Because of the unique characteristics of Zernike polynomials (i.e., there is a correspondence between Zernike coefficient and aberration), it is usually used to establish the interface of integrated optomechanical analysis [10]. For example, Chen *et al.* calculated the optical path difference (OPD) and optical aberrations through Zernike polynomials to achieve an optimum design [11]. This approach improved the optimization results of the supporting bipod flexure for a space mirror. Moreover, based on Zernike polynomial fitting, Di Varano analyzed the effect of thermal gradients and vibrations on image quality [12]. Utilizing Zernike polynomial fitting, Di Varano established an interface for the purpose of analyzing the impact of optical element deformation on optical performance, which is a simple and convenient way for design and optimization of an airborne camera.

In this paper, based on FEA and optical system analysis of airborne cameras, an integrated analysis method was proposed to design and analyze optical and mechanical structures. The objective of this work is to research the influence of microvibration on the accuracy of the optical surface. Another objective is to investigate the impact of microvibration on the optical performance of airborne cameras. This paper performed a comprehensive performance analysis, including lens surface errors, modulation transfer function (MTF), etc. It mainly studied the effect of microvibration on optical performance. The focus is on the following aspects: (a) Based on FEA data, the rigid body displacement of the optical element was calculated. (b) Based on the data of distortion, the accuracy of deformed surface was evaluated by peak to valley (PV) and root mean square (RMS). (c) The effect of microvibration on optical performance by integrated optomechanical analysis was examined.

In Section 2, the optical system and camera structure were designed. In Section 3, an FEA was performed to compute the deformations of the optical element and verify the dynamic response of the airborne camera. In Section 4, the surface distortion data in the optical system were obtained through data processing. RMS and PV were used to evaluate the surface accuracy. In Section 5, the FEA data were fitted by Zernike polynomials. Then, the responses of the optical system were calculated and analyzed under dynamic and static conditions. Finally, the analysis results were verified through experiments.

Table 1. Parameters of Optical System

Parameters	Value
Object distance (mm)	infinity
Wavelengths (nm)	420–760
Focal length (mm)	80
F#	8
FOV (°)	28
MTF (at 91 lp/mm)	>0.32
Distortion	<1%
Glass type	H-ZBAF50, H-F13, H-ZK6, H-ZK20, F2

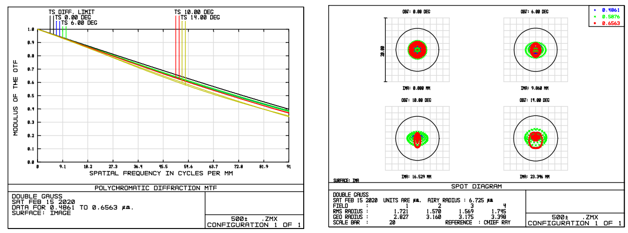

(a) (b)

Fig. 1. Optical performance of simulation. (a) MTF diagram; (b) spot diagram.

2. OPTICAL SYSTEM AND CAMERA STRUCTURE

A. Optical System

In this paper, the optical system parameters are shown in Table 1 [13].

The optical performance of the system under ideal conditions is shown in Fig. 1. The results show that the system meets the optical requirements under ideal conditions. To analyze the optical performance, the Airy diameter and the diffraction limit are shown in the spot diagrams and the MTF diagrams, respectively. The MTF diagram does not show a significant difference to the diffraction limit for all fields. For a spot diagram, all rays are concentrated in a circle (i.e., the Airy diameter). The radius of Airy, largest RMS, and largest geometric (GEO) radius are 6.725, 1.745, and 3.398 μm, respectively.

B. Camera Structure

The airborne camera's size is 120 mmL $*$ 95 mmW $*$ 62 mmH, and its weight is 1.5 kg, including lens, holder, connector part 1, connector part 2, and CCD, as illustrated in Fig. 2(a). Figure 2(b) shows the lens component, which includes six pieces of lens.

In the lens mounting stage, the change of surface accuracy is measured by an interferometer. However, it is difficult to track the surface accuracy of optical elements after barrel assembly. Therefore, the objectives of this paper are to obtain the optical element deformation and analyze the impact of the deformation on the optical performance by simulation analysis. An optomechanical analysis is developed, as shown in Fig. 3.

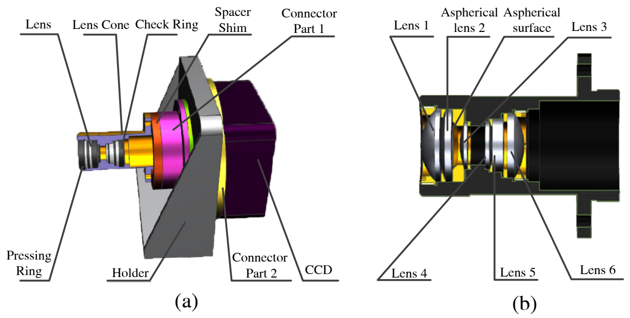

Fig. 2. (a) Camera structure diagram; (b) lens diagram.

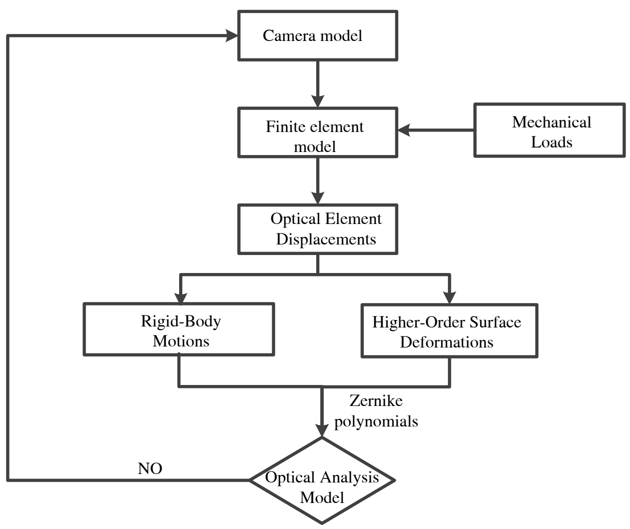

Fig. 3. Optomechanical analysis interaction.

3. CAMERA FEA

The deformation of the optical element of airborne cameras is affected by many factors (e.g., temperature fluctuations, vibration, gravity). To predict the deformation, the finite element (FE) model is established, as shown in Fig. 4. There are 384,721 nodes and 325,360 elements in the FE model. Table 2 shows the material properties of the airborne camera, in which the material of the lens barrel and the main structure of the camera are aluminum alloy, and the material of lenses 1 to 6 are H-ZBAF50, H-F13, H-ZK6, H-ZK20, F2, and H-ZBAF50, respectively.

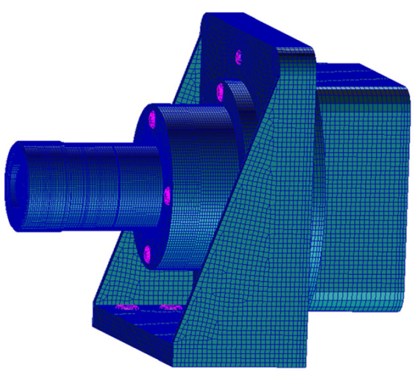

Fig. 4. Finite element model of airborne camera.

Table 2. Material Properties in the Model

Material	Density (kg/m^3)	Poisson's Ratio	Elastic Modulus (Mpa)
H-ZBAF50	3.77	0.279	85920
H-F13	2.69	0.231	83540
H-ZK6	3.54	0.267	82530
H-ZK20	3.66	0.271	76940
F2	3.50	0.231	57400
Al alloy	2.81	0.330	72000

Table 3. Load Conditions

Condition	Acceleration of X (g)	Acceleration of Y (g)	Acceleration of Z (g)
1	3	0	0
2	0	3	0
3	0	0	3

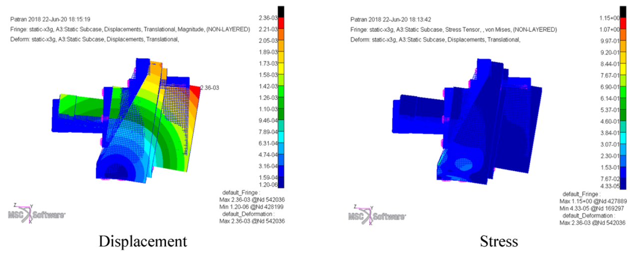

Fig. 5. Displacement and stress diagram in Condition 1.

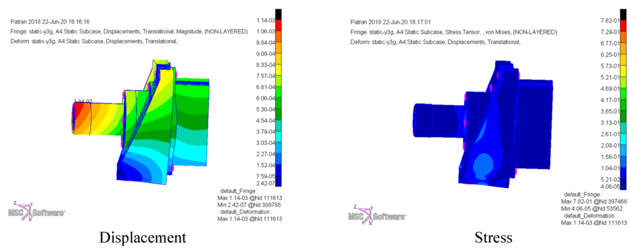

Fig. 6. Displacement and stress diagram in Condition 2.

A. Static Analysis

To verify the performance of the airborne camera under static load, the static analysis is performed by the MSC Nastran. In this paper, the three loads in Table 3 are analyzed separately, and the surface data are extracted for optical performance analysis.

The results of the static analysis are shown in Figs. 5–7. The maximum stresses and displacements are given in Table 4. As shown in the results, the maximum stress of the airborne camera is 2.17 Mpa under a load of (0, 0, 3 g), which is less than the allowable stress of the material. The maximum displacement of the airborne camera is 6.24e-3 mm, which is less than the given tolerance. The maximum stress and displacement appear in condition 3; therefore, we perform surface fitting based on the displacement data of condition 3 to calculate the rigid body displacement, surface accuracy, and static response of the optical system.

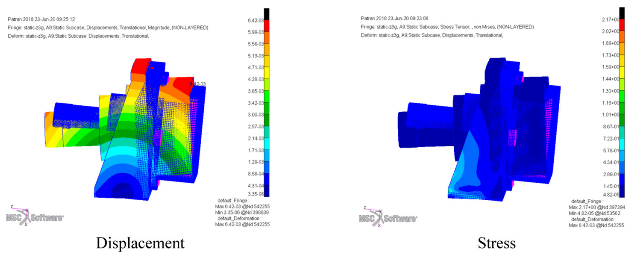

Fig. 7. Displacement and stress diagram in Condition 3.

Table 4. Static Analysis Results

States	Maximum Stress (Mpa)	Maximum Displacement (mm)
1	1.15	2.26e-3
2	7.82e-1	1.14e-3
3	2.17	6.24e-3

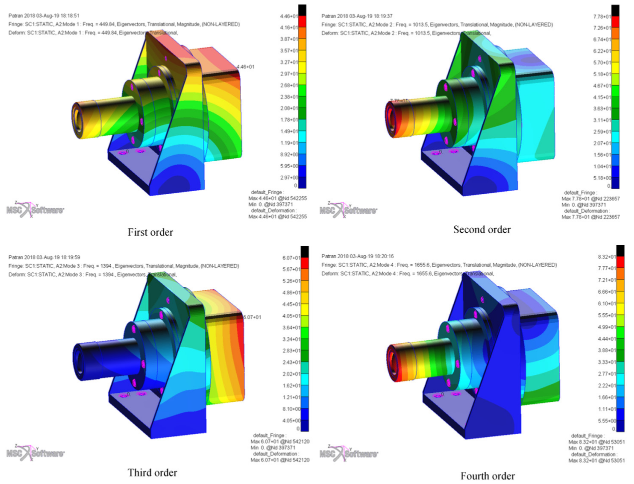

Fig. 8. First four modes.

Table 5. First Six Natural Frequencies

Order	First	Second	Third	Fourth	Fifth	Sixth
Frequency (Hz)	499.8	1013.5	1394.0	1655.6	2100.5	2439.3

B. Modal Analysis

Modal analysis is the foundation of the camera structure design. The structure of the camera is significantly affected by the natural frequencies and dynamic response of the camera assembly. By strengthening the structural components, the natural frequency of the camera can be increased to avoid resonance. Their effect can be seen in the first four mode shapes of the structure with natural frequencies of 499.98, 1034.2, 1673.5, and 1781.8 Hz, as shown in Fig. 8. The first six natural frequencies are shown in Table 5. The natural frequency of the camera is higher than the requirement of 400 Hz, which is well above the working frequency of the camera.

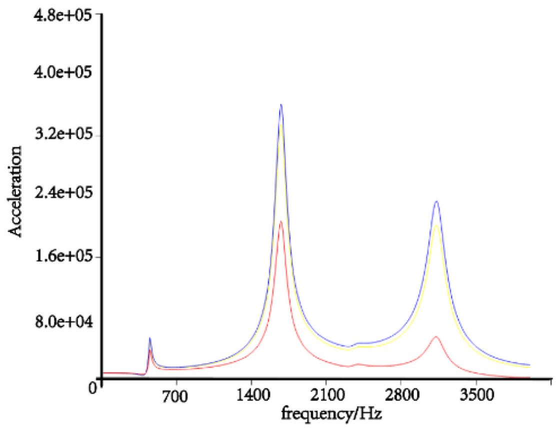

Fig. 9. Frequency response of X.

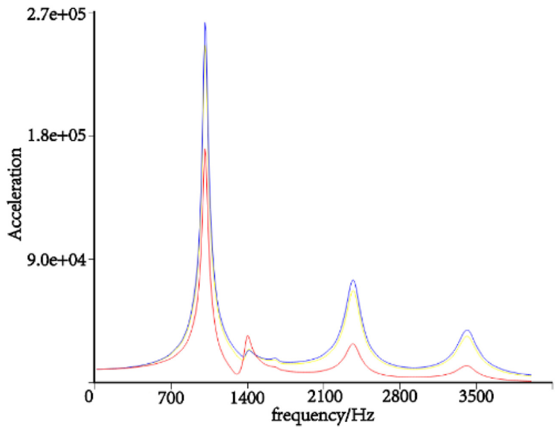

Fig. 10. Frequency response of Y.

C. Frequency Response Analysis

To calculate the dynamic response of the camera structure at different frequencies and verify the accuracy of modal analysis, frequency response analysis is performed under acceleration of 9.8 m/s^2 in x, y, and z for the airborne camera. Figures 9–11 show the results of the frequency response analysis of lenses 1–3. As can be seen from the results, the peak appears at 490, 1010, and 1660 Hz, which verified the modal analysis results.

D. Transient State Analysis

Transient state analysis can obtain the response of displacement, stress, and strain. In this paper, the transient state analysis under the sinusoidal load is used as the microvibration excitation to analyze the influence of microvibration on the optical performance. Transient state analysis is performed under a 490 Hz displacement load. The load of transient state analysis is shown in Eq. (1),

$$x(t) = A\sin(\omega t)$$

$$\omega = 2\pi f, \tag{1}$$

where A is the amplitude, and the value is 12 μm. f is the excitation load frequency, and the value is 490 Hz. Displacement-time response curves of Lens 1 are shown in Figs. 12–14. It can be seen

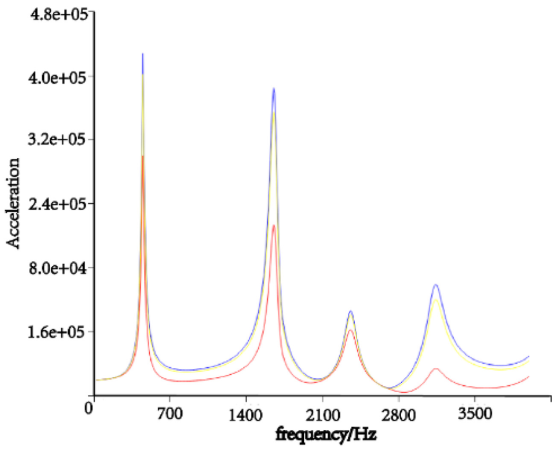

Fig. 11. Frequency response of Z.

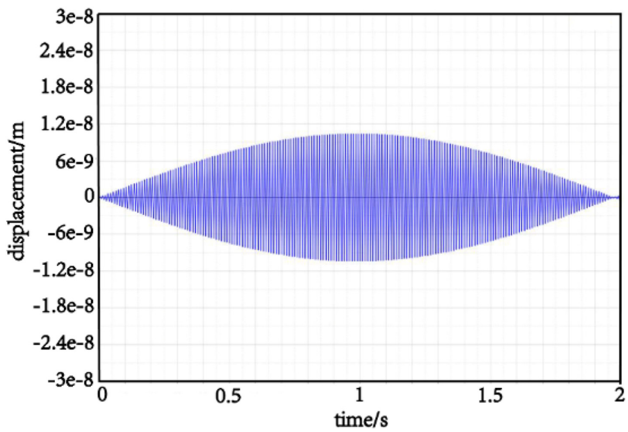

Fig. 12. Displacement-time response of X.

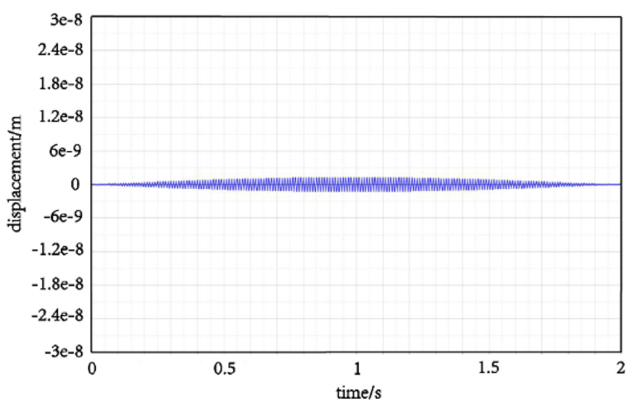

Fig. 13. Displacement-time response of Y.

from the simulation results that the displacement-time response in the z direction is much larger than that of x and y. Therefore, it is necessary to optimize vibration reduction in the z direction.

The response of the optical element is obtained through transient state analysis. In order to analyze the effect of microvibration on optical performance, the displacement data of the surface of the optical element are extracted.

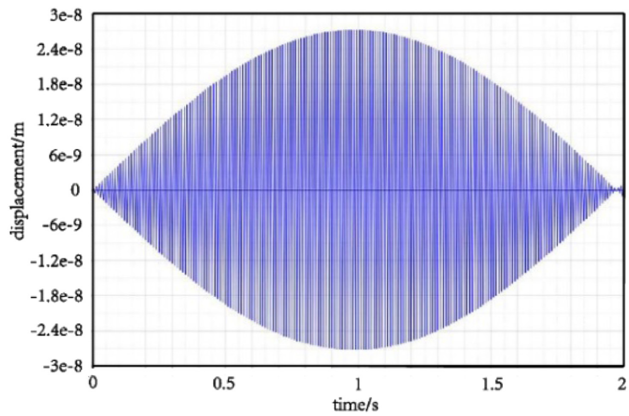

Fig. 14. Displacement-time response of Z.

4. FEA DATA PROCESSING

A. Calculation of Rigid Body Displacement of Optical Element

The displacement data of the surface of the optical element in FEA includes two parts (i.e., rigid body displacement and surface distortion). To analyze the accuracy of the optical surface, the rigid body displacement must be removed. The rigid body displacement is expressed as homogeneous coordinate transformation. Assume (x_i, y_i, z_i) are the coordinates of $O - xyz$ and (x_i', y_i', z_i') are the coordinates of $O' - xyz$. The relationship between (x_i, y_i, z_i) and (x_i', y_i', z_i') is as follows:

$$\left(x_i', y_i', z_i', 1\right)^T = A_{4\times4}(x_i, y_i, z_i, 1)^T, \tag{2}$$

where $A_{4\times4}$ is a matrix of homogeneous coordinate transformation, and $(x_i', y_i', z_i', 1)^T$ and $(x_i, y_i, z_i, 1)^T$ are the homogeneous coordinates in $O' - xyz$ and $O - xyz$, respectively. The matrix of translation and the rotation are expressed as Eqs. (3) and (4),

$$T = \begin{bmatrix} 1 & 0 & 0 & a \\ 0 & 1 & 0 & b \\ 0 & 0 & 1 & c \\ 0 & 0 & 0 & 1 \end{bmatrix} \quad R_x = \begin{bmatrix} 1 & 0 & 0 & 0 \\ 0 & \cos\theta_x & -\sin\theta_x & 0 \\ 0 & \sin\theta_x & \cos\theta_x & 1 \\ 0 & 1 & 1 & 1 \end{bmatrix}, \tag{3}$$

$$R_y = \begin{bmatrix} \cos\theta_y & 0 & \sin\theta_y & 0 \\ 0 & 1 & 0 & 1 \\ -\sin\theta_y & 0 & \cos\theta_y & 0 \\ 0 & 0 & 0 & 1 \end{bmatrix} \quad R_Z = \begin{bmatrix} \cos\theta_z & -\sin\theta_z & 0 & 0 \\ \sin\theta_z & \cos\theta_z & 0 & 1 \\ 0 & 0 & 1 & 0 \\ 0 & 0 & 0 & 1 \end{bmatrix}, \tag{4}$$

where a, b, and c are the translation in the direction of x, y, and z, and θ_x, θ_y, and θ_z are the rotating angle about x, y, and z, respectively. Then, the equation for matrix A can be written as

$$A = T * R_x * R_y * R_z. \tag{5}$$

The rotating angle of the optical element is very small (i.e., θ is infinitely close to 0). As a result, we obtain Eq. (6),

$$\begin{cases} \cos\theta_x = \cos\theta_y = \cos\theta_z = 1 \\ \sin\theta_x \approx \theta_x,\ \sin\theta_y \approx \theta_y,\ \sin\theta_z \approx \theta_z \end{cases}. \tag{6}$$

Applying Eq. (6) in (5), matrix A can be expressed as

$$A' = \begin{bmatrix} 1 & -\theta_z & \theta_y & a \\ \theta_x * \theta_y + \theta_z & -\theta_x * \theta_y * \theta_z + 1 & -\theta_x & b \\ -\theta_y + \theta_x * \theta_z & \theta_y * \theta_z + \theta_x & 1 & c \\ 0 & 0 & 0 & 1 \end{bmatrix}. \quad (7)$$

Because the rotating angle is infinitely close to *0* (i.e., the quadratic and higher-order terms in matrix A' can be approximately 0), then the matrix A' can be expressed as

$$A' = \begin{bmatrix} 1 & -\theta_z & \theta_y & a \\ \theta_z & 1 & -\theta_x & b \\ -\theta_y & \theta_x & 1 & c \\ 0 & 0 & 0 & 1 \end{bmatrix}. \quad (8)$$

Suppose that $(\Delta x_i, \Delta y_i, \Delta z_i)$ are the surface distortion of node i. (x_i, y_i, z_i) and (x_i', y_i', z_i') are the coordinates of the initial node and the deformed node, respectively. The relationship between (x_i, y_i, z_i) and (x_i', y_i', z_i') is shown in Eq. (9),

$$\begin{bmatrix} x_i' \\ y_i' \\ z_i' \\ 1 \end{bmatrix} = \begin{bmatrix} 1 & -\theta_z & \theta_y & a \\ \theta_z & 1 & -\theta_x & b \\ -\theta_y & \theta_x & 1 & c \\ 0 & 0 & 0 & 1 \end{bmatrix} \begin{bmatrix} x_i \\ y_i \\ z_i \\ 1 \end{bmatrix} + \begin{bmatrix} \Delta x_i \\ \Delta y_i \\ \Delta z_i \\ 0 \end{bmatrix}. \quad (9)$$

Then, the surface distortion can be expressed as

$$\begin{cases} \Delta x_i = x_i' - x_i + \theta_z y_i - \theta_y z_i - a \\ \Delta y_i = y_i' - y_i + \theta_z x_i + \theta_x z_i - b \\ \Delta z_i = z_i' - z_i + \theta_y x_i - \theta_x y_i - c \end{cases}. \quad (10)$$

To calculate the parameters of θ_x, θ_y, θ_z, a, b, and c by the least square method, the objective function is established, as shown in Eq. (11),

$$Q = \sum_{i=1}^{n} \begin{bmatrix} \left(x_i' - x_i + \theta_z y_i - \theta_y z_i - a\right)^2 \\ +\left(y_i' - y_i + \theta_z x_i + \theta_x z_i - b\right)^2 \\ +\left(z_i' - z_i + \theta_y x_i - \theta_x y_i - c\right)^2 \end{bmatrix}, \quad (11)$$

where Q is the target value. The value of Q reflects the accuracy of the fit. To make the fitted surface closest to the actual deformed surface, we need to find the minimum of Q. According to extreme conditions, Eq. (12) can be obtained by taking the derivative of unknown parameters. Then, the rigid body displacements can be solved by simultaneous equations in Eq. (12). Based on the displacement data under Condition 3 in Section 3.A, the rigid body displacement of the optical element is solved, as shown in Table 6,

$$\begin{matrix} \frac{\partial Q}{\partial a} = 0 & \frac{\partial Q}{\partial b} = 0 & \frac{\partial Q}{\partial c} = 0 \\ \frac{\partial Q}{\partial \theta_x} = 0 & \frac{\partial Q}{\partial \theta_y} = 0 & \frac{\partial Q}{\partial \theta_z} = 0 \end{matrix}. \quad (12)$$

As shown in Table 6, the maximum translation in the direction of x, y, and z are $-1.652\text{e-}04$, 1.466e-06, and $-2.145\text{e-}04$, which all appear on the first lens. For rotation, θ_z is significantly greater than θ_x and θ_y. It is necessary to improve the method of circumferential fixation of the optical element. From the impact on optical performance, a, b, c, θ_x, and θ_y will cause the optical axis to deflect, which has a greater impact on optical performance than θ_z. Therefore, it is important to reduce the rigid body displacement to improve the optical performance of the airborne camera.

Table 6. Rigid Body Displacement

Lens	a/mm	b/mm	c/mm	θ_x	θ_y	θ_z
1	–1.65e-04	1.46e-06	–2.14e-04	5.79e-07	–1.47e-04	6.09e-01
2	–1.44e-04	1.38e-06	–2.14e-04	5.79e-07	–1.47e-04	7.89e-01
3	–1.33e-04	1.34e-06	–2.14e-04	5.78e-07	–1.48e-04	3.02e-01
4	–1.06e-04	1.23e-06	–2.14e-04	5.79e-07	–1.48e-04	2.24e-01
5	–1.04e-04	1.22e-06	–2.14e-04	5.78e-07	–1.49e-04	2.36e-01
6	–8.99e-05	1.12e-06	–2.14e-04	5.62e-07	–1.48e-04	2.25e-02

B. Surface Accuracy Evaluation

Discrete points on the optical surface are extracted and a point set P (x_i, y_i, z_i) is generated. To get the spherical parameters of (a, b, c, R), the least square method is used to fit a spherical surface based on discrete data. The standard fitted spherical equation can be written as Eq. (13). (a, b, c) are the center coordinates of P_0, and R is the radius of the spherical surface,

$$(x-a)^2 + (y-b)^2 + (z-c)^2 = R^2. \quad (13)$$

To solve the spherical parameters of (a, b, c, R) by the method of least squares, an objective function, as shown in Eq. (14), is constructed,

$$L = \sum_{i=1}^{n} \left[\frac{(x_i-a)^2 + (y_i-b)^2 + (z_i-c)^2 - R^2}{2R}\right]^2. \quad (14)$$

The objective function can be written as follows:

$$L = [A(x_i^2 + y_i^2 + z_i^2) + Bx_i + Cy_i + Dz_i + E]^2, \quad (15)$$

where $2AR = 1$, $Aa = -B$, $2Ab = -C$, $2Ac = -D$, and $E = (a^2 + b^2 + c^2 - R^2)/2R$. The constraint of the equation is $B^2 + C^2 + D^2 - 4AE = 1$. The Lagrange function with constraint can be expressed as

$$L = \left[A(x_i^2 + y_i^2 + z_i^2) + Bx_i + Cy_i + Dz_i + E\right]^2 + \lambda(B^2 + C^2 + D^2 - 4AE - 1). \quad (16)$$

According to the extreme conditions, Eq. (17) can be obtained,

$$\begin{matrix} \frac{\partial L}{\partial A} = 0 & \frac{\partial L}{\partial B} = 0 & \frac{\partial L}{\partial C} = 0 \\ \frac{\partial L}{\partial D} = 0 & \frac{\partial L}{\partial E} = 0 & \frac{\partial L}{\partial \lambda} = 0. \end{matrix} \quad (17)$$

Intermediate variables of (A, B, C, D, E) can be obtained by the equation simultaneously in Eq. (17). Then, the spherical parameters of (a, b, c, R) can be obtained from intermediate variables.

Surface distortion $\Delta P_i(\Delta x_i, \Delta y_{i,} \Delta z_i)$ can be obtained by removing rigid body displacement. Let $P' = \{P_i'(x_i', y_i', z_i')|i = 1, 2, 3, \cdots\}$ be the intersection of the line connecting point $P = \{P_i(x_i, y_i, z_i)|i = 1, 2, 3, \cdots\}$ with the center P_0 and the fitted sphere. Then, the point $P_f = \{P_{fi}(x_i' + \Delta x_i, y_i' + \Delta y_{i,} z_i' + \Delta z_i)|i = 1, 2, 3, \cdots\}$ is obtained by adding P' and ΔP. Spherical parameters of (a, b, c, R) of the distortion surface can be obtained by performing a least squares operation based on the data of P_f. Define a collection of $\Delta di = \{\delta d_i \,|i = 1, 2, 3, \cdots\}$, where $\delta d_i = |P_{fi} P_0 - R|$. RMS and PV can be obtained by Eq. (18),

Table 7. PV and RMS

Order	PV/nm	RMS/nm
1	22.49	3.72
2	14.36	3.19
3	33.86	8.67
4	43.89	10.73
5	60.39	10.79
6	47.39	10.77
7	10.70	2.88
8	42.62	9.57
9	61.76	15.18
10	60.51	14.30
11	21.44	4.09
12	58.69	13.75

$$\mathrm{RMS} = \sqrt{\frac{\sum_{i=1}^{n} \delta d_i}{n}}$$

$$\mathrm{PV} = \mathrm{Max}(\Delta d) - \mathrm{Min}(\Delta d). \tag{18}$$

To avoid degradation of optical performance, the maximum PV value is expected to be no more than 63.3 nm (i.e., 1/10λ, where λ = 633 nm), whereas the RMS value is expected to be no more than 21.1 nm (i.e., 1/30λ). Based on the displacement data of Condition 3 in Section 3.A, the value of PV and the RMS of the distortion surface are solved, as shown in Table 7. It can be seen from Table 7 that the PV of the surface distortion changed greatly, while the RMS changed little. The circular contact area between the retaining ring and the lens produced large deformations, resulting in a larger PV. As shown in Table 7, the maximum PV and RMS are 61.76 and 18.18 nm, both smaller than those of the requirement (63.3 and 21.1 nm). Considering the accuracy of the surface, the surface distortion caused by microvibration will not have a significant effect on optical performance.

C. Coordinate Transformation and Displacement Correction

There are different coordinate systems in the displacement of FEA and the optical system. In optical systems, coordinates are usually represented in sagittal height. However, the data of FEA are the relative displacement of the node. To fit the deformed surface, the displacement in the finite element coordinate system needs to be corrected to the optical coordinate system. The usual method is to convert the displacement of the FEA into the sagittal height of the optical surface through a displacement correction algorithm. The schematic diagram of the sagittal axial displacement is shown in Fig. 15.

Assuming P_U is the initial node, P_D is the corresponding changed node. The displacement of P_U and P_D are ΔR and ΔZ in the radial direction and optical axis, respectively. TP_D is the parameter converted from the FE deformation data to the optical axis direction. The sagittal height displacement of TP_D can be used to describe the change of optical surface. For the sagittal equation of the known optical surface, the sagittal displacement can be obtained by Eq (19). $Z = Z(R)$ is the equation of the optical surface in the sagittal direction. The displacement can be converted into the direction of the optical axis by Eq. (19),

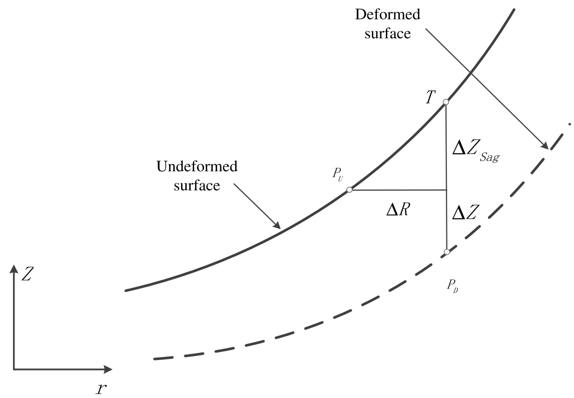

Fig. 15. Calculation of surface sag displacement.

$$\begin{cases} TP_D = \Delta Z + \Delta Z_{\mathrm{SAG}} \\ \Delta Z_{\mathrm{SAG}} = Z(R_{p0}) - Z(R_{P_0} + \Delta R) \end{cases}. \tag{19}$$

5. ZERNIKE POLYNOMIALS FITTING

A. Result of Zernike Polynomial

Because of the unique characteristics of Zernike polynomials (i.e., the relationships between Seidel aberrations and Zernike polynomials coefficients), Zernike polynomials have been widely used in integrated optomechanical analysis [14,15]. Zernike polynomials are orthogonal on a continuous unitary circle but not on a discrete unitary circle [16]. The discrete surface data set Δ can be represented by Zernike polynomials as Eq. (20),

$$\Delta = \sum_{i=0}^{\infty} a_i \phi_i = a_0 + a_1\phi_1 + a_2\phi_2 + \cdots + a_n\phi_n, \tag{20}$$

where a_i (i = 1, 2, ..., n) is the coefficient of the polynomial to be solved; Φ_i (i = 1, 2, ..., n) is the Zernike polynomial.

In this paper, to construct a set of orthogonal polynomials on the discrete unitary circle, Gram–Schmidt orthogonalization is carried out. Then, Zernike polynomials coefficients are calculated by the least square fitting method [17].

The optical element deformation is transferred into Zernike coefficients through optomechanical codes written in MATLAB. We used fringe Zernike polynomials to fit the optical element deformation and obtained the fringe Zernike coefficients. Fringe Zernike coefficients are a subset of standard

Table 8. First Nine Terms of Fringe Zernike Coefficients of Surface 1

Order	Zernike Polynomials	Aberration Name	Coefficient
1	1	piston	0.00072116925
2	$\rho\cos\theta$	X tilt	−0.00000214047
3	$\rho\sin\theta$	Y tilt	0.00000273958
4	$2\rho^2 - 1$	defocus	0.00000112253
5	$\rho^2\sin 2\theta$	pri astigmatism X	0.00000196861
6	$\rho^2\sin 2\theta$	pri astigmatism Y	−0.00000497404
7	$(3\rho^3 - 2\rho)\cos\theta$	pri coma X	−0.00000179254
8	$(3\rho^3 - 2\rho)\sin\theta$	pri coma Y	0.00000171297
9	$6\rho^4 - 6\rho^2 + 1$	pri spherical	0.00000056790

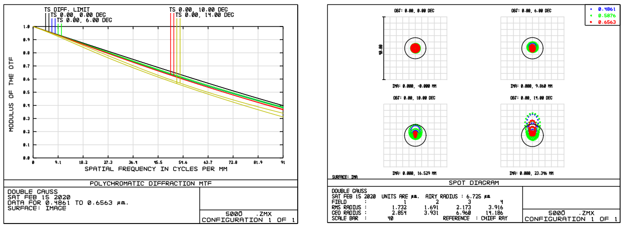

Fig. 16. Optical performance of fitted system. (a) MTF diagram; (b) spot diagram.

Table 9. Value of MTF in All Fields

Field	Initial MTF	Fitting MTF	Decline (%)
0°	0.377879	0.377458	1.2
6°	0.379748	0.372849	1.8
10°	0.364166	0.357888	7.7
14°	0.331137	0.304922	7.8

Zernike coefficients. The displacement data under Condition 3 in Section 3.A are used to perform Zernike fitting to solve the Zernike coefficient. The first nine terms of the fringe Zernike coefficients are shown in Table 8.

B. Optical Performance Analysis

Compared with PV and RMS, the response of the optical system can better reflect the influence of microvibration on optical performance. To analyze the effect of microvibration on optical performance, the displacement data are fitted by Zernike polynomials and output in optics format. Then, the optical system response is calculated to analyze the effect of microvibration on optical performance.

1. Static Analysis

The displacement data under Condition 3 in Section 3.A are used to perform Zernike fitting to solve the Zernike coefficient. Then, the response of the optical system is calculated by ZEMAX. Figure 16 is the optical performance of the fitted optical system under Condition 3. The MTF curve, compared with Fig. 1(a), does not drop significantly in all fields of view (i.e., the performance of the optical system has not decreased significantly). Compared with Fig. 1(b), the maximum RMS radius and GEO radius are 3.916 and 14.186 μm, respectively, which are larger than the 1.745 and 3.398 μm in Fig. 2. The GEO radius at 10°and 14° is more than Airy-diameter radius (i.e., there is a greater impact on the edge field of view (FOV) in Condition 3).

Table 9 shows a detailed comparison of MTF at 91lp/mm. Compared with the design requirement of 8%, the MTF declined 1.2%, 1.8%, 7.7%, and 7.8% at a FOV of 0°–14°, in which the edge FOV has a greater impact. It can be seen from the static analysis results that the designed airborne camera can meet the design requirements under the given working conditions.

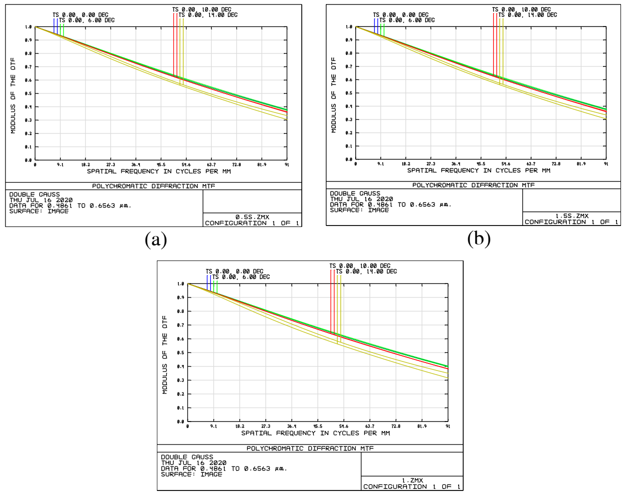

Fig. 17. MTF diagram. (a) MTF at 0.5 s; (b) MTF at 1 s; (c) MTF at 1.5 s.

2. Dynamic Analysis

Dynamic analysis studies the effect of rigid body displacement caused by microvibration on optical performance. It can be seen from Section 4.B that the influence of surface distortion on the optical performance of airborne cameras is negligible. When performing dynamic analysis, the optical element can be regarded as a rigid body. The rigid body displacement of the optical element can be calculated through the displacement data obtained by transient state analysis of Section 3.D. Based on ZEMAX simulation, the effect of the rigid body displacement at different times on optical performance can be analyzed. The MTFs of the optical system at 0.5, 1, and 1.5 s are as shown in Fig. 17. From the results of optical system response, microvibration has little effect on the optical performance of the designed small airborne camera. As can be seen from the results, there is no obvious difference in MTF between different moments. Compared with Fig. 1(a), the maximum decline of MTF is 7.30% at 0.5 s, which is within the design requirements of 8%. The results indicate that the impact of microvibration on optical performance of the designed airborne camera is small.

6. VIBRATION TEST OF AIRBORNE CAMERA

To verify the simulation analysis results, a vibration test was set up for an airborne camera. In this work, we designed two cameras with the same structure (i.e., the object distance of 500 mm and infinite object distance). In order to reduce test costs, we use a camera with an object distance of 500 mm for ground simulation experiments. To ensure the accuracy of the experimental results and the similarity of the two cameras, the design method of the camera with an object distance of 500 mm is the same as the camera with the infinite object distance. For an optical system, a camera with an object distance of 500 mm has the same design index as a camera with an infinite object distance. There is no significant change in the parameters of the optical system simulation results of the two cameras. When compared, the structure of the two cameras use the same structural design method, lens assembly method, and the same number of

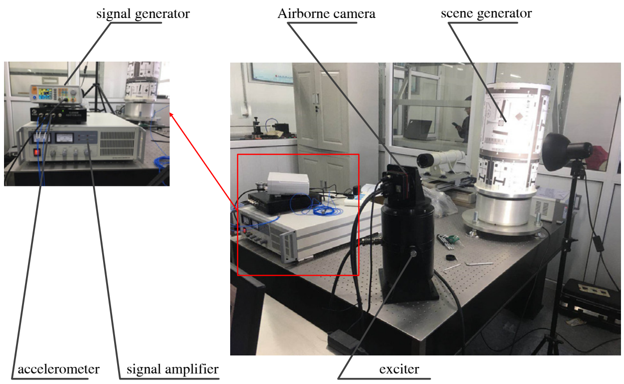

Fig. 18. Experimental setup for airborne camera.

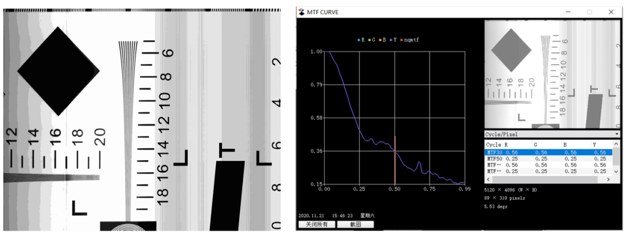

Fig. 19. Image without vibration.

lenses and materials. The purpose of this experiment is to verify whether the decline of the image MTF is consistent with the simulation analysis trend. As shown in Fig. 18, an object consisting of ISO12233 was imaged by the camera under test, and the image quality of the camera was analyzed. The camera was placed in the environmental test chamber, as shown in Fig. 18, which was subjected to vertical microvibration loads. The experimental device was composed of an exciter, a signal amplifier, a signal generator, an airborne camera, an accelerometer, a scene generator, and a PC. The exciter provided the required vibration for the experiment, and sinusoidal vibration signals of different frequencies were generated by a signal generator.

The test process under microvibration was as follows:

(1) keeping the environment without microvibration and measuring MTF;
(2) keeping the environment with microvibrations of 300, 400, 500, and 600 Hz, then measuring the MTF of the camera system.

Figure 19 shows the test image without microvibration. Figure 20 shows the imaging results at the frequencies of 300, 400, 500, and 600 Hz, respectively. From the imaging results, there was no significant difference in the image with or without microvibration. To clearly show the influence of microvibration on the image quality, the image results were analyzed to obtain its MTF.

Based on the edge method, spatial frequency response (SFR) analysis of the image is performed through the image analysis software iQstest, and the analysis result is shown in Fig. 21.

As can been seen from the experimental results, there was no significant impact on the optical performance of the designed small airborne camera, which was consistent with the simulation results in Section 5. The MTF experimental data of the camera

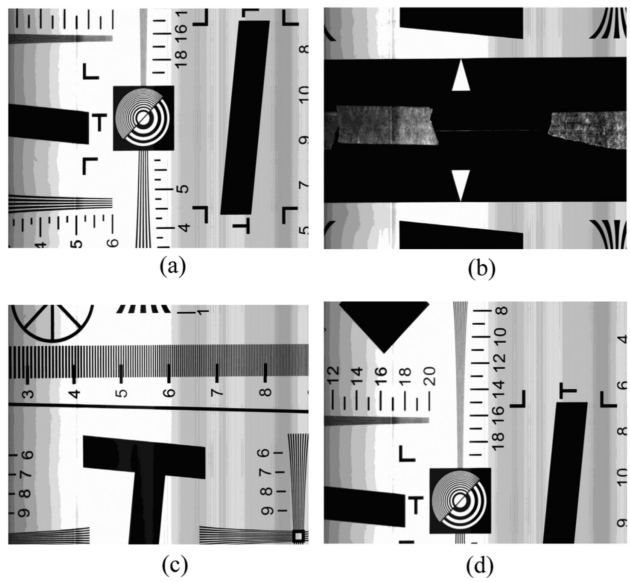

Fig. 20. Image results. (a) 300 Hz; (b) 400 Hz; (c) 500 Hz; (d) 600 Hz.

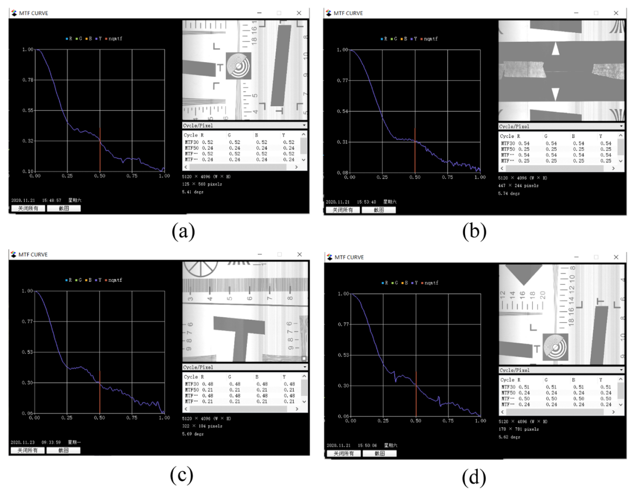

Fig. 21. Analysis result of image. (a) 300 Hz; (b) 400 Hz; (c) 500 Hz; (d) 600 Hz.

system are shown in Table 10, which shows the relative decline percentage of the MTF compared to Fig. 19. As can be seen from Table 10, the variations of the system MTF under different experimental microvibrations were small, and the maximum relative decline of MTF30 and MTF50 were 14% and 16%, respectively. Compared with the MTF of the optical system, the MTF of the camera after barrel mount will decrease. Therefore, the decrease in MTF measured by the test will be greater than the simulation analysis result. However, its downward trend is consistent with the simulation results.

To further verify the imaging results of the designed airborne camera under microvibration, the vibration device and camera with infinite object distance were used to perform imaging tests on distant buildings. As shown in Fig. 22, (a) is the imaging result without vibration, and (b) is the imaging result when the vibration frequency is 490 Hz. As shown in Fig. 22, the resolution of Fig. 22(b) does not decrease significantly, and the

Table 10. Measuring Results of MTF

Frequency	300 Hz	400 Hz	500 Hz	600 Hz
MTF30	0.52	0.54	0.48	0.51
MTF50	0.24	0.25	0.21	0.24
Decline of MTF30 (%)	7%	3.5%	14%	8.9%
Decline of MTF50 (%)	4%	0	16%	4%

(a) (b)

Fig. 22. Image results for buildings. (a) is the imaging result without vibration, and (b) is the imaging result when the vibration frequency is 490 Hz.

image quality can still meet the design requirements, which is consistent with the analysis results.

7. CONCLUSION

For rapid estimation of optical behavior, we develop a more complex integrated analysis method to analyze the optomechanical system, which allows us to get more comprehensive performance analysis insights. This paper analyzed the effect of microvibration on the optical performance of the airborne camera by integrated optomechanical analysis, which provided guidance for the predesign of the airborne camera. The results of this investigation indicated that the microvibration had no significant effect on the optical system performance of the designed small airborne camera. Based on the results of this study, the main conclusions can be drawn as follows:

(1) Data processing was an important step in analyzing the effect of microvibration on the accuracy of the optical surface. The data of surface distortion were the basic data for the analysis, which need to be obtained by removing the rigid body displacement from the FEA displacement data.

(2) To analyze the change in surface accuracy, the data of surface distortion were fitted utilizing the least squares method. It can be seen from the results that both PV and RMS were within the given tolerance of the design. The circular contact area between the retaining ring and the lens produced large deformations, resulting in a larger PV. In all surfaces, the maximum of PV and RMS were 61.76 and 15.18, respectively, both smaller than those of the requirement.

(3) Optical performance was analyzed under static and dynamic conditions. Simulation results of ZEMAX shown that the MTF of the optical system was reduced by a maximum of 7.8% under given conditions, which were smaller than the requirement of 8%. Then, the dynamic analysis of the airborne camera was completed by solving the effects of rigid body displacement at different times on the optical performance. The results show there are no significant changes in MTF at different times, and the maximum decline is 7.3%. Finally, the vibration experimental results show that the camera meets the imaging requirements under the experimental vibration load.

Funding. Science and Technology Development Projects of Jilin Province (20190302065GX, 20200703033ZP); Micro-Nano and Ultra-Precision Key Laboratory of Jilin Province (20140622008JC); Capital construction budget funds of Jilin Province (2020C022-2); Key Projects of Jilin Province Talent Development Fund.

Disclosures. The authors declare that there are no conflicts of interest related to this article.

REFERENCES

1. W. Liu, Y. Xu, Y. Yao, Y. Xu, H. Shen, and Y. Ding, "Relationship analysis between transient thermal control mode and image quality for an aerial camera," Appl. Opt. **56**, 1028–1036 (2017).
2. F. Maamar and A. Boudjemai, "Optomechanical optimal design configuration and analysis of glue pad bonds in lens mounting for space application," Adv. Space Res. **65**, 2263–2275 (2020).
3. Y.-C. Chen, B.-K. Huang, Z.-T. You, C.-Y. Chan, and T.-M. Huang, "Optimization of lightweight structure and supporting bipod flexure for a space mirror," Appl. Opt. **55**, 10382–10391 (2016).
4. Z. Zhang, H. Wang, X. Quan, G. Pei, M. Tian, T. Liu, K. Long, P. Li, and Y. Rong, "Optomechanical analysis and performance optimization of large-aperture KDP frequency converter," Opt. Laser Technol. **109**, 633–642 (2018).
5. L. Weiyi, D. Yalin, W. Qingwen, J. Jiqiang, G. Liang, and W. Linghua, "Thermal analysis and design of the aerial camera's primary optical system components," Appl. Therm. Eng. **38**, 40–47 (2012).
6. P. Rausch, S. Verpoort, and U. Wittrock, "Unimorph deformable mirror for space telescopes: design and manufacturing," Opt. Express **23**, 19469–19477 (2015).
7. C. C. Barrera, P. Zuluaga, and R. Restrepo, "Analysis of optomechanical method for materials selection in optical design," in *Latin America Optics & Photonics Conference* (2016).
8. Z.-P. Xue, C.-X. Wang, Y. Yu, P.-P. Wang, H.-Y. Zhang, Y. Sui, M. Li, and Z.-Y. Luo, "Integrated optomechanical analyses and experimental verification for a thermal system of an aerial camera," Appl. Opt. **58**, 6996–7005 (2019).
9. K. B. Doyle, V. L. Genberg, and G. J. Michels, "Integrated optomechanical analysis of adaptive optical systems," Proc. SPIE **5178**, 20–28 (2004).
10. W. Swantner and W. W. Chow, "Gram-Schmidt orthonormalization of Zernike polynomials for general aperture shapes," Appl. Opt. **33**, 1832–1837 (1994).
11. C. Yi-Cheng, H. Bo-Kai, Y. Zhen-Ting, C. Chia-Yen, and H. Ting-Ming, "Optimization of lightweight structure and supporting bipod flexure for a space mirror," Appl. Opt. **55**, 10382–10391 (2016).
12. I. Di Varano, "Characterization of optical aberrations induced by thermal gradients and vibrations via Zernike and Legendre polynomials," Opt. Photon. J. **6**, 113–123 (2016).
13. J. Lin, H. Wang, Y. Gu, A. Yi, J. Wang, and Z. Yang, "Design, analysis and preliminary tests of a linear array CCD aerial camera for ground simulation," Optik **200**, 163378 (2019).
14. L. Hanshin, "Use of Zernike polynomials for efficient estimation of orthonormal aberration coefficients over variable noncircular pupils," Opt. Lett. **35**, 2173–2175 (2010).

15. S. Singh and D. Ganotra, "Wavefront fitting and comparison of camera aberrations using Zernike circle polynomials," Optik **124**, 2379–2386 (2013).
16. F. Dai, Y. Zheng, Y. Bu, and X. Wang, "Zernike polynomials as a basis for modal fitting in lateral shearing interferometry: a discrete domain matrix transformation method," Appl. Opt. **55**, 5884–5891 (2016).
17. Z. Wang, O. Chee, W. Qu, and Q. Xu, "A new method for improving the accuracy of wavefront fitting with Zernike polynomials," Phys. Procedia **19**, 134–138 (2011).